




# Rapid coating of asphalt to prepare carbon-encapsulated composites of nano-silicon and graphite for lithium battery anodes

Wenping Liu<sup>1,2</sup> , Huarui Xu<sup>1,\*</sup>, Haiqing Qin<sup>2</sup>, Yanlu Lv<sup>3</sup>, Guisheng Zhu<sup>1</sup>, Xiaoxu Lei<sup>2</sup>, Feng Lin<sup>2,3</sup>, Zhenjun Zhang<sup>2</sup>, and Lihui Wang<sup>2</sup>

<sup>1</sup> School of Mechanical and Electrical Engineering, Guangxi Key Laboratory of Information Materials, Guilin University of Electronic Technology, Guilin 541004, China

<sup>2</sup> Guilin Key Laboratory of Microelectronic Electrode Materials and Biological Nanomaterials and National Special Mineral Materials Engineering Technology Research Center and Guangxi Key Laboratory of Superhard Materials, China Nonferrous Metal (Guilin) Geology and Mining Co., Ltd, Guilin 541004, China

<sup>3</sup> College of Materials Science and Engineering, Guilin University of Technology, Guilin 541004, China

Received: 25 October 2019

Accepted: 16 December 2019

Published online:

23 December 2019

© Springer Science+Business Media, LLC, part of Springer Nature 2019

## ABSTRACT

In order to obtain large-scale industrial silicon/carbon composites as anode materials for lithium-ion batteries, graphite-loaded nano-silicon (G@Si) composite was synthesized by a facile spray drying method, and then asphalt powders were fast fused on the surface and carbonized at 1100 °C for 2 h to obtain core-shell G@Si@C composite. The nano-Si particle was pinned on the graphite surface without bareness via asphalt carbon layer. The G@Si@C composite delivers excellent electrochemical performance with an initial reversible charge capacity of 502.5 mAh g<sup>-1</sup> and coulombic efficiency of 87.5%, and the capacity retention is 83.4% after 400 cycles. The superior cycle performance is attributed to the carbon layer relieving volume change, stabilizing SEI film and inhibiting particle pulverization. Moreover, the outstanding high-rate discharge properties of G@Si@C composite may be owing to the preferable electrochemistry kinetics such as fast charge transfer and lithium-ion diffusion.

## Introduction

Lithium-ion batteries (LIBs) have been explored into the most concerning reversible energy storage batteries in the past decades due to long cycle life and high energy density with low self-discharge [1–3]. However, the energy density of LIBs using graphite

as anode material already cannot satisfy the demands for new-energy vehicles and consuming electronics products [4, 5]. One method to improve the energy density of LIBs is to explore anode materials with high lithium storage capacity. Dahn and co-workers have done quite a lot of work on silicon-based electrodes as lithium anode material in the late 1990s

Address correspondence to E-mail: xuhuarui@163.com

[6, 7]. Chan [8] and Zhang [9] have simulated the electrochemical lithiation and delithiation of crystalline silicon and silicon-carbon multilayer films with first principles to provide firm conceptual foundations for future design of improved Si-based anodes for Li-ion battery applications. Silicon has been supposed to be a promising anode material to replace graphite in Li-ion batteries due to its high theoretical capacity (3579 mAh/g for  $\text{Li}_{15}\text{Si}_4$ ), low lithiation potential (below 0.5 V vs.  $\text{Li}/\text{Li}^+$ ) and the abundance in the earth [10–14]. However, there is a large volumetric variation ( $\sim 300\%$ ) during the lithium insertion and extraction into/from pure silicon anode material, which is easy to form unstable solid electrolyte interphase (SEI) film and destroy the electrode, leading to rapid decay of cycle life [15–18].

In order to promote commercial application of the Si-based anode material, there are many researches on solving these issues. The main method is to prepare Si-based nano-composites with other materials, such as graphite [19, 20], carbon materials [21],  $\text{TiO}_2$  [22],  $\text{Co}_3\text{O}_4$  [23] and  $\text{SiO}_x$  [24]. Zhu [25] and Huang [26] have designed the carbon-coated Si-based composite as an anode material with electrochemical performance for lithium-ion batteries. Many studies have reported silicon/carbon composite materials as lithium battery anodes, but low-cost industrial production is crucial [26–29]. Because graphite and carbon materials can buffer the stress caused by the huge volume variation and enhance conductivity of silicon, the way to combine nano-Si with graphite and coat carbon layer to prepare G@Si@C composite materials is easy to realize industrialization. Chen et al. [30, 31] have prepared carbon-coated graphite/plasma nano-silicon with a core-shell structure as lithium-ion battery anode materials by facile spray drying method, which is very easy to industrialize. But in their experiment, the used solvent tetrahydrofuran is flammable, combustible and high cost, hindering the practical application of asphalt-carbon-coated Si-based anode. It is very necessary to explore other facile methods to coat asphalt carbon layer on nano-Si for industrialization.

In this work, we have prepared nano-Si particles via inductively coupled plasma (ICP) technology, which is promising for industrialization. The G@Si composite was obtained by the facile spray drying. The asphalt layer has been coated with asphalt powders by fast fusing method and carbonized to

obtain G@Si@C composite for LIBs anode material, which can realize low cost and fast preparation. We have combined many structure and morphology characterization techniques with cyclic voltammetry and electrochemical impedance spectroscopy to investigate the effect of the asphalt carbon coating layer on the improving performance of G@Si@C composite anode. The G@Si@C composite exhibits an initial reversible charge capacity of  $502.5 \text{ mAh g}^{-1}$  and coulombic efficiency of 87.5%, with a capacity retention of 83.4% after 400 cycles, suggesting that G@Si@C composite is an excellent anode for LIBs.

## Experiment

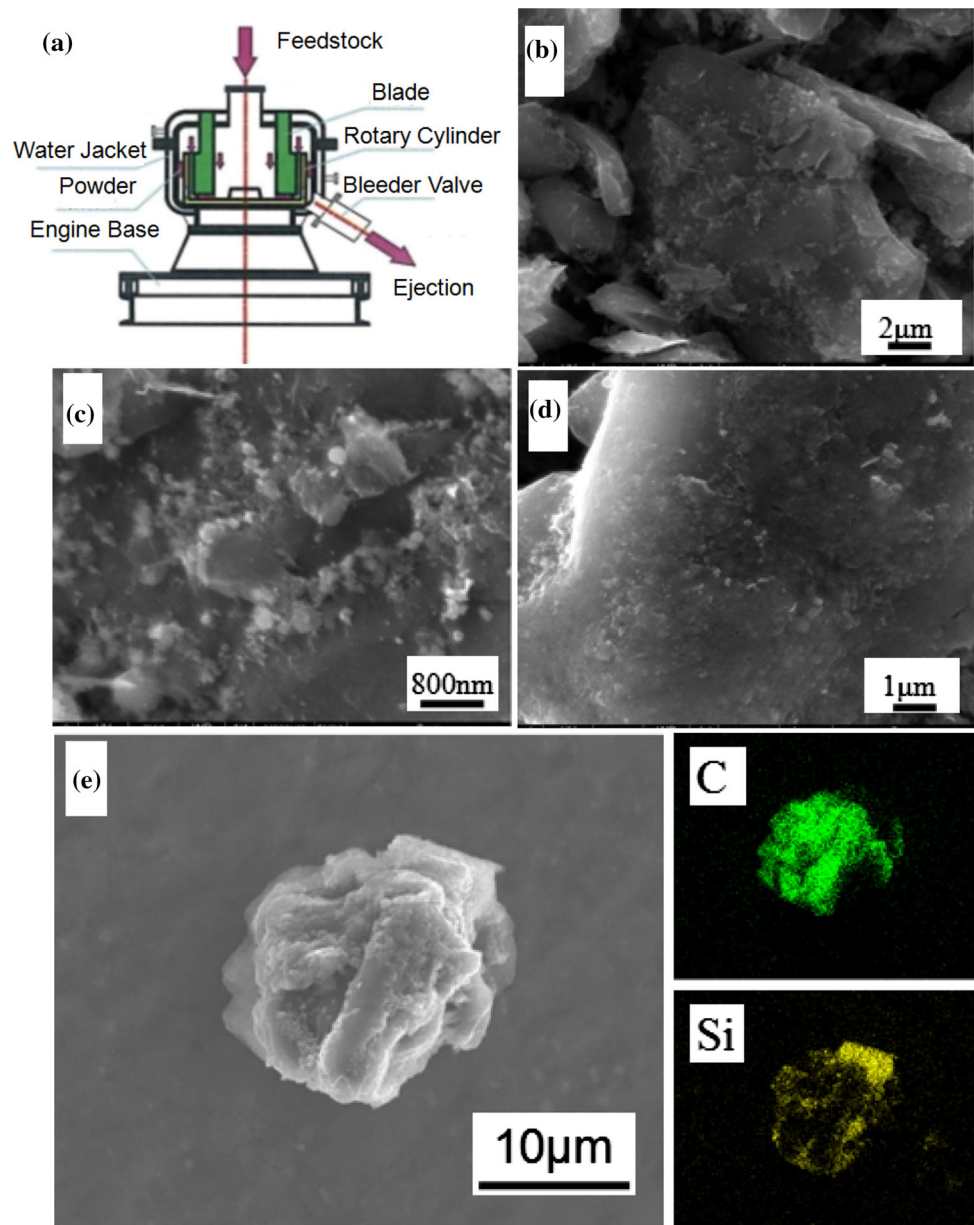
### Sample preparation

Nano-Si powders were prepared by the 15 KW inductively coupled plasma (ICP) equipment, which was purchased from Tekna Plasma System Inc. (Canada). 10 wt% Nano-Si powders, 85 wt% artificial graphite and 5 wt% citric acid were added into deionized water and mixed into a suspension with a solid content of 30 wt%. The G@Si composite precursor powders were obtained by drying the suspension with spray drying method. Then, 85 wt% G@Si composite precursor powders and 15 wt% asphalt powders were put into the fusion machine and fused 10 min with 2000 r/min to obtain G@Si@C composite precursor powders. The structural representation of the fusion machine is shown in Fig. 1a. The powders were squeezed by the high-speed revolution of rotary cylinder in the fusing process, so an asphalt layer was formed on the surface of G@Si composite precursor powders. Finally, the G@Si and G@Si@C precursor powders were heat-treated at  $1100 \text{ }^\circ\text{C}$  under vacuum for 2 h to obtain G@Si and G@Si@C composite.

### Sample characterization

The structure and morphology of samples were investigated by field emission electron microscopy (FE-SEM; Quanta 200), transmission electron microscopy (TEM; JEM-2100HR), X-ray diffraction (XRD; D8 ADVANCE) and Raman spectroscopy (Jobin Yvon LabRam HR800). The silicon content in the composite was confirmed by thermogravimetric analysis/differential scanning calorimetry (TGA/

**Figure 1** a The structural representation of fusion machine, b–c G@Si composite and d G@Si@C composite, e EDS mapping of G@Si@C composite.



DSC, DSC-204 phoenix). The specific surface area was measured by Brunauer–Emmett–Teller (BET) test with Micromeritics ASAP-2020M nitrogen adsorption.

### Electrochemical measurements

The electrochemical performances of the samples were studied by 2032 coin half-cells, which were assembled in an argon-filled glove box. The cells were composed of working electrode, Celgard 2400 as the separator, lithium foil as a reference electrode and solution of 1 M LiPF<sub>6</sub> in ethylene carbonate(EC)/

diethyl carbonate(DEC)/ ethylene carbonate(EMC) (1:1:1, v/v) as the electrolyte. The working electrode was obtained by coating well-mixed slurry on a copper foil and dried at 80 °C under vacuum for 24 h. The slurry was prepared by scattering 80 wt% active powders material, 10 wt% carbon black and 10 wt% binder in pure water. The weight ratio of 3:2 for butadiene styrene rubber and carboxymethyl cellulose was used as the binder.

The charge/discharge tests were performed on a LAND CT2001A battery test system at 25 °C. The charge/discharge method to evaluate cycling performance was conducted as follows: the cell firstly

was discharged to 0.01 V at current density of 100 mA g<sup>-1</sup>, then discharged to 0.005 V at low current density of 10 mA g<sup>-1</sup> and finally charged to 1.5 V at current density of 100 mA g<sup>-1</sup>. The high-rate discharge ability was tested at current density for 100, 200, 400, 800, 1200, 1600 and 2000 mA g<sup>-1</sup> after the cell has been activated for 10 cycles with the charge/discharge method mentioned above. Cyclic voltammetry (CV) and impedance spectroscopy (EIS) were conducted on the Solartron 1287 electrochemical workstation. The scan rate of CV is 0.1 mV s<sup>-1</sup> with a voltage range from 1.5 to 0.005 V, and the frequency range of EIS is from 100 kHz to 10 mHz.

## Results and discussion

The SEM images of G@Si composite and G@Si@C composite are shown in Fig. 1. It can be found that the nano-Si powders are evenly distributed on the surface of graphite as shown in Fig. 1b, c. After asphalt carbon coating, the nano-Si powders are firmly pinned on the graphite surface without bareness, as shown in Fig. 1d. Energy-dispersive X-ray spectroscopy of G@Si@C composite is shown in Fig. 1e, and it can be found that silicon is carried on the carbon base. The specific surface area of nano-Si, graphite, G@Si composite and G@Si@C composite is shown in Table 1. It can be found that the specific surface area of G@Si composite is 5.57 m<sup>2</sup> g<sup>-1</sup>, but the specific surface area obviously decreases after asphalt carbon coating G@Si@C composite is only 2.19 m<sup>2</sup> g<sup>-1</sup>, which is close to graphite with 1.81 m<sup>2</sup> g<sup>-1</sup>.

The TEM image in Fig. 2a displays that the nano-Si powders are spherical nanoparticles and the nano-Si particles are interspersed on the graphite in G@Si composite as shown in Fig. 2b. Figure 2c and d represents that a carbon layer is formed on the surface of the nano-Si particle and graphite, which is helpful to release volume expansion during the insertion of lithium-ion and enhance electrical conductivity. The selected area electron diffraction (SAED) image of single nano-Si particle in Fig. 2d shows that the nano-Si particle is monocrystal, and the electron diffraction spots of Si (111), Si (220) and Si (311) are presented in

the figure. As shown in Fig. 3h, the SAED image of G@Si@C composite manifests the monocrystal electron diffraction spots of nano-Si particle and polycrystalline electron diffraction ring C (002) and C (004) of graphite [25].

The X-ray diffraction with copper K $\alpha$  radiation was used to analyze the structural characteristic of nano-Si, graphite and G@Si@C composite. As presented in Fig. 3a, the peaks at 26.4°, 42.2°, 44.4°, 54.5°, 59.7° and 77.2° are assigned to the lattice planes (002), (100), (101), (004), (103) and (110) of graphite (cubic phase: JCPDS# 041-487), and the peaks at 28.4°, 47.3°, 56.1°, 69.1° and 76.4° correspond to the lattice planes (111), (220), (311), (400) and (331) for silicon (cubic phase: JCPDS# 00-027-1402) [30, 32–34]. Compared to nano-Si and graphite, SiC or SiO<sub>2</sub> are not observed in G@Si@C composite, which means that there is no production of those compounds during the synthesis processes [34, 35]. According to the main peak at 2 $\theta$  = 28.4°, the crystalline diameter of nano-Si powders can be calculated using the Scherrer equation as follows [36]:

$$d = \frac{0.9\lambda}{\beta * \cos \theta} \quad (1)$$

where  $d$  is the crystal size of synthesized silicon,  $\lambda$  is the wavelength of the X-ray diffraction, and  $\beta$  is the full-width at half-maximum peak (FWHM) of the XRD pattern. It can be calculated that the crystalline diameter value of nano-Si powders is 49 nm. The results of TEM confirm that the nano-Si powders are spherical monocrystalline particles, so the average particle size of nano-Si powders is 49 nm.

The Raman spectrum of nano-Si, graphite and G@Si@C composite is further employed to determine the structure as shown in Fig. 3c. The sharp peaks around 512 cm<sup>-1</sup> and 905 cm<sup>-1</sup> are assigned to the crystalline silicon [31, 36, 37]. The peaks at 1343 cm<sup>-1</sup> and 1578 cm<sup>-1</sup> correspond to amorphous carbon band  $sp^3$  of the D band (disordered structure) and graphitic carbon  $sp^2$  of the G band (ordered structure), respectively [30, 31, 38]. The value of  $I_D/I_G$  is used to evaluate the degree of graphitization. Graphite displays high  $I_D/I_G$  (0.18), which means that the graphite has a high degree of graphitization.

**Table 1** The specific surface area of nano-Si, graphite, G@Si composite and G@Si@C composite

Sample	Nano-Si	Graphite	G@Si composite	G@Si@C composite
BET surface area (m <sup>2</sup> g <sup>-1</sup> )	41.07	1.81	5.57	2.19



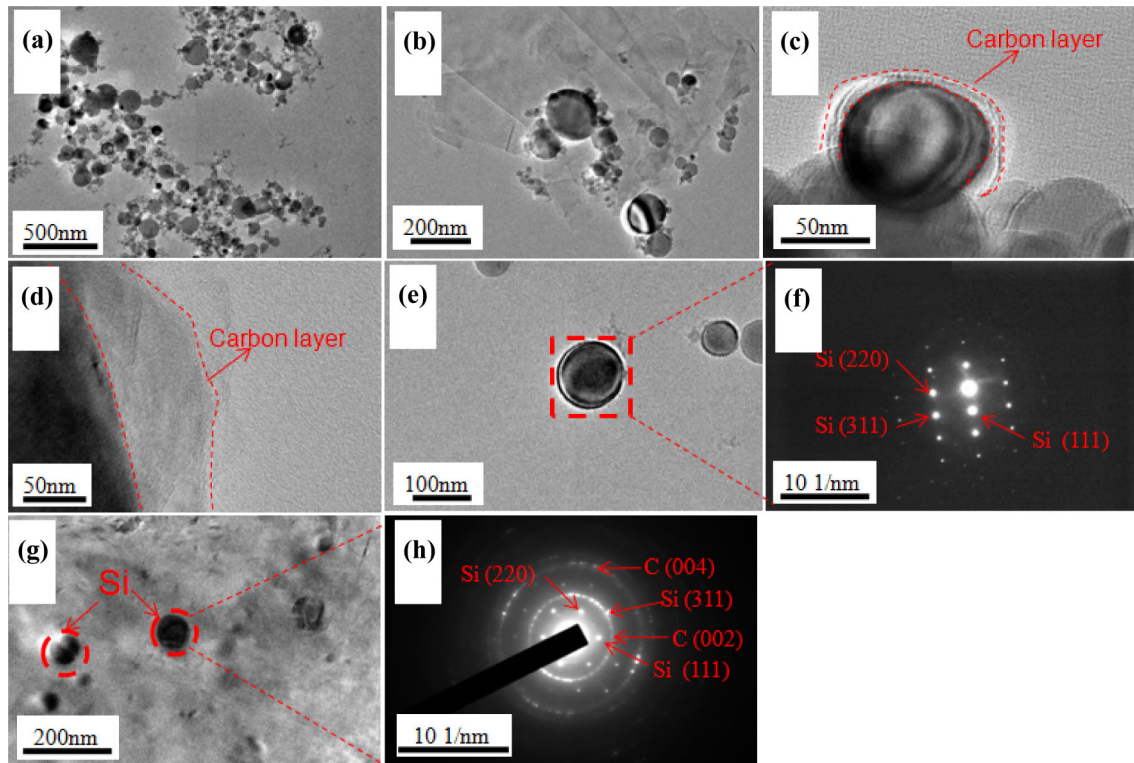
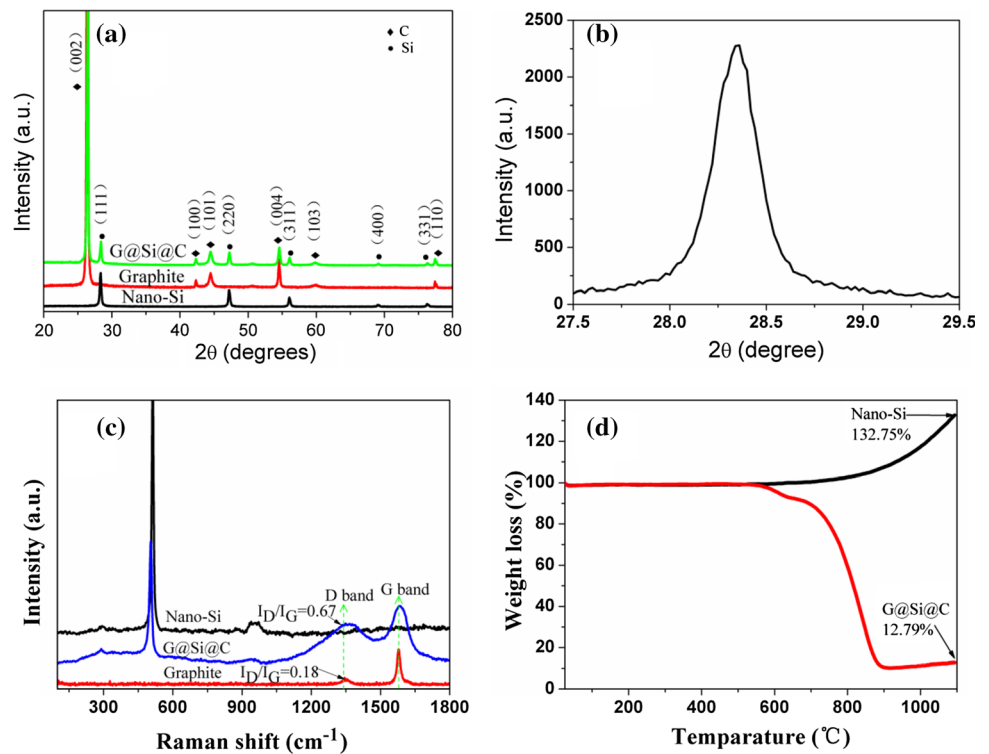


**Figure 2** TEM images of **a** nano-Si, **b** G@Si composite and **c–d** G@Si@C composite; the SAED images of **c–f** nano-Si and **g–h** G@Si@C composite.

**Figure 3** **a** XRD pattern of nano-Si, graphite and G@Si@C composite, **b** major XRD peak at  $28.4^\circ$  of nano-Si, **c** Raman spectra of nano-Si, graphite and G@Si@C composite, and **d** TGA curves of nano-Si and G@Si@C composite.



However, the value of  $I_D/I_C$  in G@Si@C composite increases to 0.67, indicating the asphalt carbon is disorder structure.

In order to confirm the silicon content in G@Si@C composite, the thermal gravimetric analysis was performed from room temperature to 1100 °C with a heating rate of 10 °C min<sup>-1</sup> in air atmosphere. As shown in Fig. 3d, the weight of nano-Si increases to 132.75% since the silicon is oxidized to silicon oxide, while the weight of G@Si@C composite decreases to 12.79% because of the combustion of asphalt carbon and graphite [20]. According to the results of TGA, the silicon content in G@Si@C composite is approximately calculated to be 9.63% (12.79/132.75%), which is roughly close to the proportion of the original nano-Si input in the synthesis process.

The cycling performance of nano-Si, graphite, G@Si composite and G@Si@C composite is shown in Fig. 4a. The initial discharge/charge capacities of nano-Si are 3519.4 and 2063.7 mAh g<sup>-1</sup> with initial coulombic efficiency of 58.6%, respectively. After 400 cycles, the reversible capacity of nano-Si is only 43.4 mAh g<sup>-1</sup>, which is mainly due to the volume expansion leading to the loss of electrical contact of nano-Si particle and destroying the electrode structure [39]. The initial discharge/charge capacities of graphite are 355.1 and 334.4 mAh g<sup>-1</sup> with an initial coulombic efficiency of 94.2%, respectively. The reversible capacity at 400th cycle is 337.7 mAh g<sup>-1</sup>, and the cycle life is very stable. For the G@Si composite, the initial discharge/charge capacities are 636.1 and 566.0 mAh g<sup>-1</sup> with an initial coulombic efficiency of 89.0%, respectively. The reversible capacity at the 400th cycle is 421.2 mAh g<sup>-1</sup>, and the capacity retention is 74.4%. Because the graphite can relieve the volume expansion of nano-Si, the cyclic life of G@Si composite is improved compared to pure nano-Si electrode [40–43]. After asphalt carbon coating, the initial discharge/charge capacities of G@Si@C composite are 574.4 and 502.5 mAh g<sup>-1</sup> with an initial coulombic efficiency of 87.5%, respectively. The existence of amorphous carbon leads to little loss of initial coulombic efficiency. However, the asphalt carbon layer can firmly pin the nano-Si particles on the surface of graphite, protect active materials from pulverization and stabilize SEI films [43]. The capacity retention of G@Si@C composite after 400 cycles is 83.4%, and the cycle life is signally improved compared to G@Si composite. Figure 4b shows the high-rate discharge capacity of

graphite, G@Si composite and G@Si@C composite, and it can be found that the addition of nano-Si is benefit to improve the high-rate discharge ability. Furthermore, asphalt carbon layer can further enhance the electrical conductivity, so the high-rate discharge ability of G@Si@C composite is superior. The first charge/discharge curves of nano-Si, graphite, G@Si composite and G@Si@C composite are shown in Fig. 4c, the discharge/charge curves of nano-Si electrode show a discharge voltage plateau around 0.1 V, corresponding to the formation of lithium-silicon alloys, and the charge voltage plateau gradually rises to 0.5 V, corresponding to the deintercalation of lithium ion from lithium-silicon alloy. Compared to charging curve of graphite, there are double charge voltage plateau in G@Si composite and G@Si@C composite because of the different lithium deintercalation voltage of graphite and silicon [44]. The discharge/charge curves at different cycle of G@Si composite and G@Si@C composite are shown in Fig. 4d and e. The consistency of discharge/charge curves for G@Si@C composite is better than for G@Si composite, which is mainly because the asphalt carbon layer can effectively relieve the volume expansion and fix nano-Si on the surface of graphite, helping to maintain the perfect electrode structure.

The scanning electron microscope and energy-dispersive X-ray spectroscopy were used to further investigate the electrode structural stability and SEI films of G@Si composite and G@Si@C composite electrodes after 400 cycles. Figure 5a and b shows the SEM images of G@Si composite and G@Si@C composite electrodes, respectively. There are distinctly discernible fractures in the G@Si composite and G@Si@C composite electrodes. The fracture in G@Si@C composite electrode is suppressed, since asphalt carbon layer is beneficial to relieve the electrode expansion. The C, Si, O and F element mapping is presented in Fig. 5c and d; the O and F element mapping of G@Si@C composite electrode is obviously less than that of G@Si composite electrode, indicating that the carbon layer stabilizes the SEI films and reduces the forming of SEI films.

The cyclic voltammetry tests with a voltage range from 0.005 to 1.5 V at a scanning rate of 0.1 mV s<sup>-1</sup> were conducted to research the electrochemical behavior of nano-Si, graphite, G@Si composite and G@Si@C composite electrodes, and the initial five-cycle CV curves were displayed in Fig. 6. The CV curves of nano-Si are presented in Fig. 6a. There is a

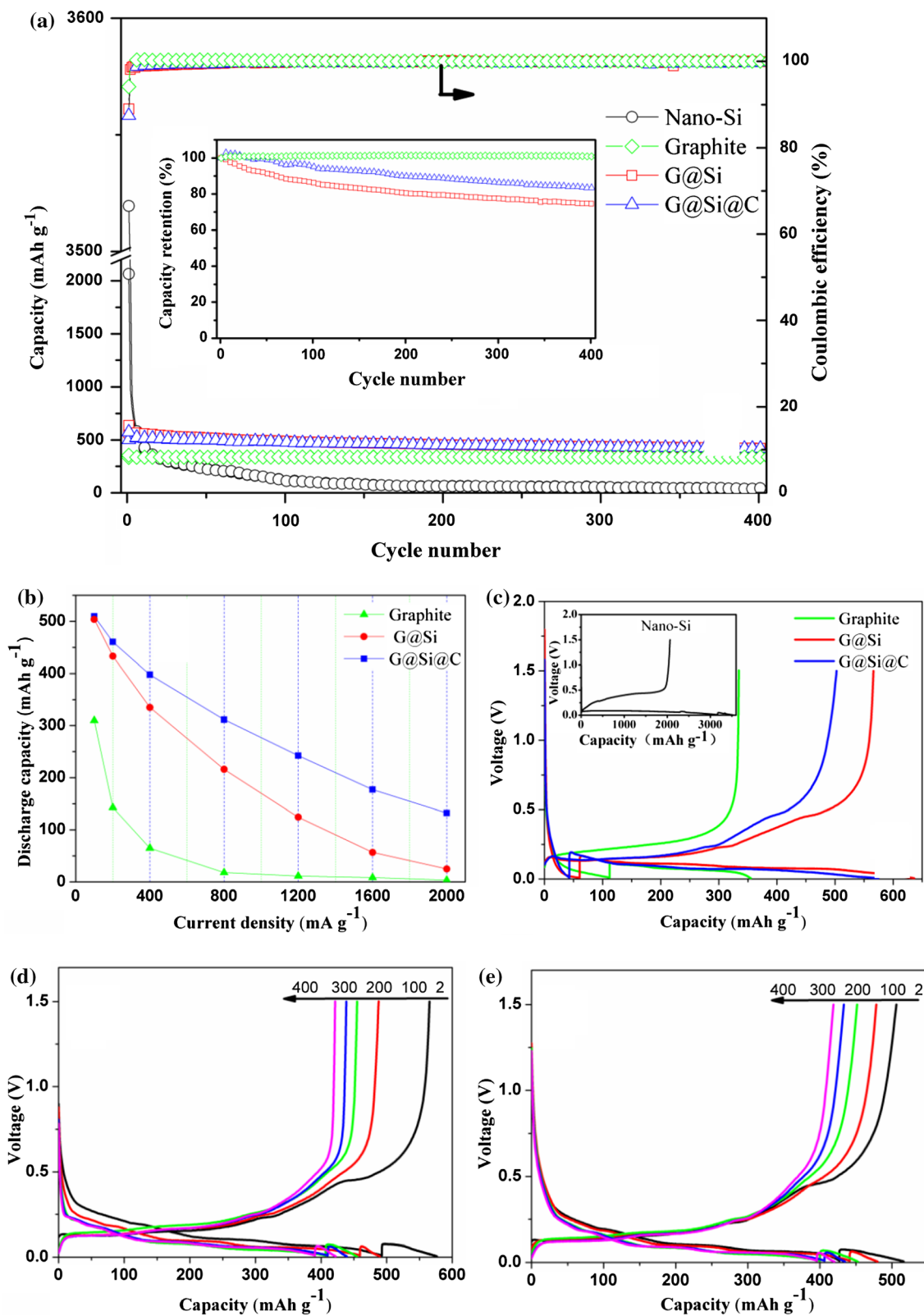
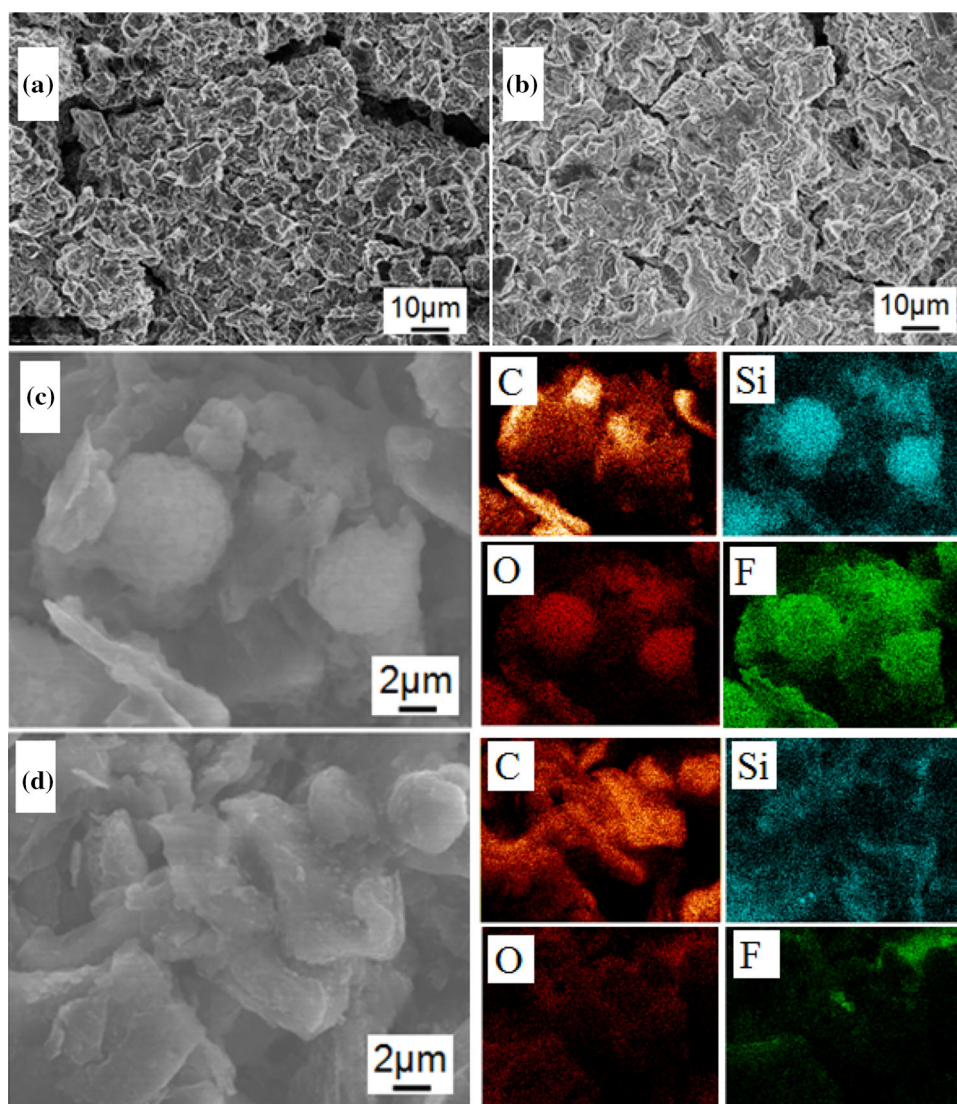


**Figure 4** a Cycling performance of nano-Si, graphite, G@Si composite and G@Si@C composite; b the high-rate discharge capacity of graphite, G@Si composite and G@Si@C composite;

c the first charge/discharge curves of nano-Si, graphite, G@Si composite and G@Si@C composite; discharge/charge curves of d G@Si composite and e G@Si@C composite.



**Figure 5** SEM images of **a** G@Si composite and **b** G@Si@C composite electrodes after 400 cycles; EDS mapping of **c** G@Si composite and **d** G@Si@C composite electrodes after 400 cycles.



sharp cathodic peak 0.1 V, corresponding to the lithiation of crystalline silicon [22]. However, there are two peaks at about 0.2 V and below 0.1 V in the later cycles because of the transformation from crystalline silicon into amorphization silicon after first lithiation [45–47]. In the anodic scan, there are two strong oxidation peaks at 0.31 and 0.50 V, which are ascribed to the reversible dealloying process of  $\text{Li}_x\text{Si}$  alloy. Compared with the CV curves of nano-Si, graphite, G@Si composite and G@Si@C composite electrodes, it can be found that the CV curves of graphite electrode exhibit a good overlap after the first cycle activation, indicating a stable cyclic performance. Moreover, the CV curves of G@Si@C composite electrode have a smaller change than those of the nano-Si and G@Si composite electrodes, which

indicates that the cycle performance of G@Si@C composite is better than that of nano-Si and G@Si composite. The result is consistent with variation of the cycle performance.

The electrochemical impedance spectra of G@Si composite and G@Si@C composite electrodes after 10, 20, 30 and 40 cycles are fitted by equivalent circuit to further investigate the electrode structure change, which are shown in Fig. 7, and the fitting result is listed in Table 2. In the equivalent circuit, The  $R_s$  is relative to contact resistance, which responds to the contact situation of active material particles [30]. It can be found that the values of  $R_s$  for G@Si composite and G@Si@C composite electrodes gradually increase with increasing the cycle number, which indicates that the contact of active material particles becomes



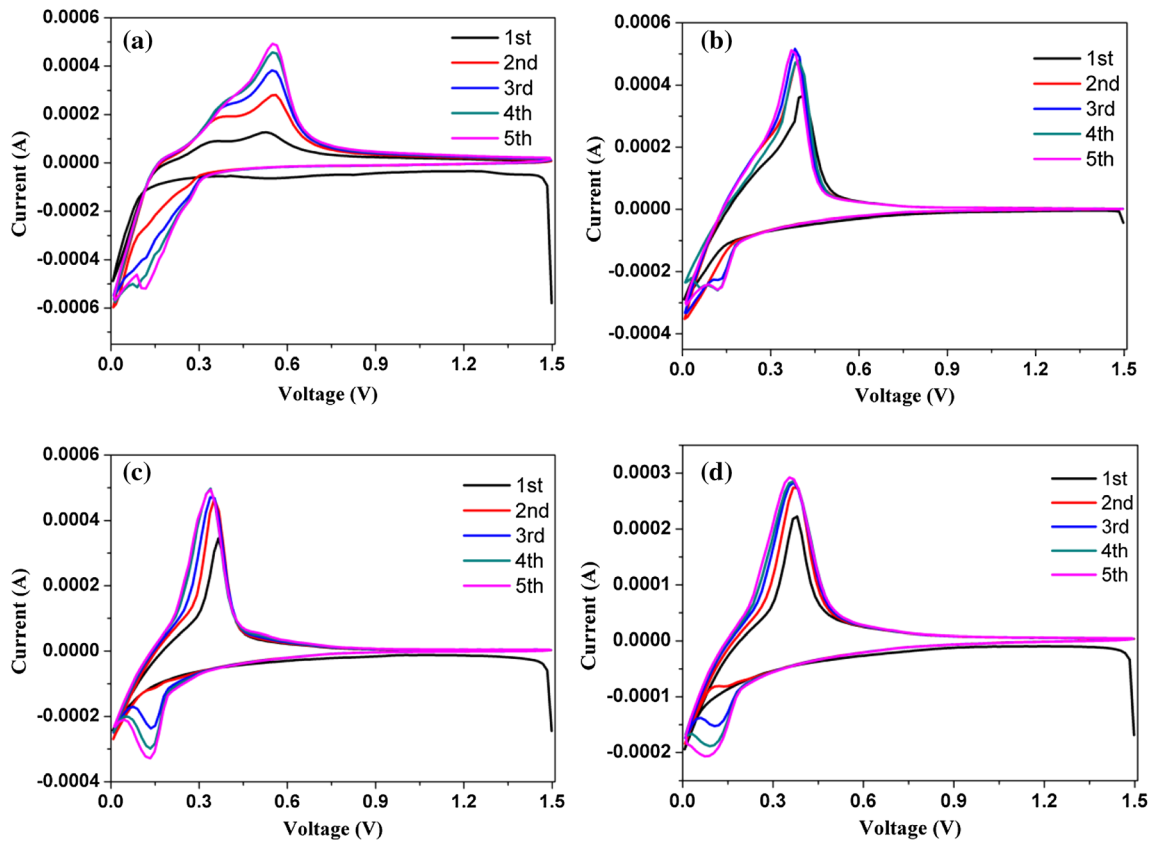


**Figure 6** CV curves of **a** nano-Si, **b** graphite, **c** G@Si composite and **d** G@Si@C composite electrodes at a scanning rate of  $0.1 \text{ mV s}^{-1}$ .

weak because of the reduplicative volume change. However, the value of  $R_s$  for G@Si@C composite electrode is less than for G@Si composite electrode, since the carbon layer can relieve the volume change. Furthermore, the first semicircle in high-frequency part corresponds to the variation of the SEI films ( $R_f$ ) [48, 49]. The value of  $R_f$  for G@Si composite electrode is obviously increasing with increasing the cycle number, indicating that the exposed nano-Si particles on the surface are easy to form the unstable films, while the  $R_f$  value of G@Si@C composite electrode is slightly variable from 20 cycles to 40 cycles, which is due to that the carbon layer on the surface is helpful to form stable films. The less volume change and stable SEI films of G@Si@C composite electrode can help to maintain perfect electrode structure, so the cycle performance of G@Si@C composite is superior to G@Si composite. The semicircle in middle-frequency part is corresponding to the charge transfer resistance ( $R_{ct}$ ) on the electrode-electrolyte interface [30, 31]. It can be found that the semicircle of G@Si composite electrode is divided into two semicircles, which are relative to the charge transfer resistance of

graphite ( $R_{ct1}$ ) and nano-Si ( $R_{ct2}$ ), respectively. The graphite particles are pulverized with the increase in cycle numbers, which is benefit to improve charge transfer area leading to the  $R_{ct1}$  value decreases, the unstable SEI films are constantly forming on the surface of nano-Si, so the  $R_{ct2}$  value gradually increases. Because carbon layer combines graphite and nano-Si as an integral particle, there is only a charge transfer semicircle for G@Si@C composite electrode. The  $R_{ct}$  value corresponding to the semicircle diminishes with the increase in cycle numbers, indicating that the particles also have pulverization. But the variation of  $R_{ct}$  value for G@Si@C composite electrode is much less than for G@Si composite electrode, which means that the carbon layer can protect the particle from pulverization to improve cycle performance. Moreover, the less  $R_{ct}$  value of G@Si@C composite electrode means better charge transfer than that of G@Si composite electrode. The straight line in the low-frequency region is responding to lithium-ion diffusion behavior in the electrode, the fitting slope between  $Z'$  and  $\omega^{-1/2}$  in low-frequency region is listed in Table 2. The facile slope

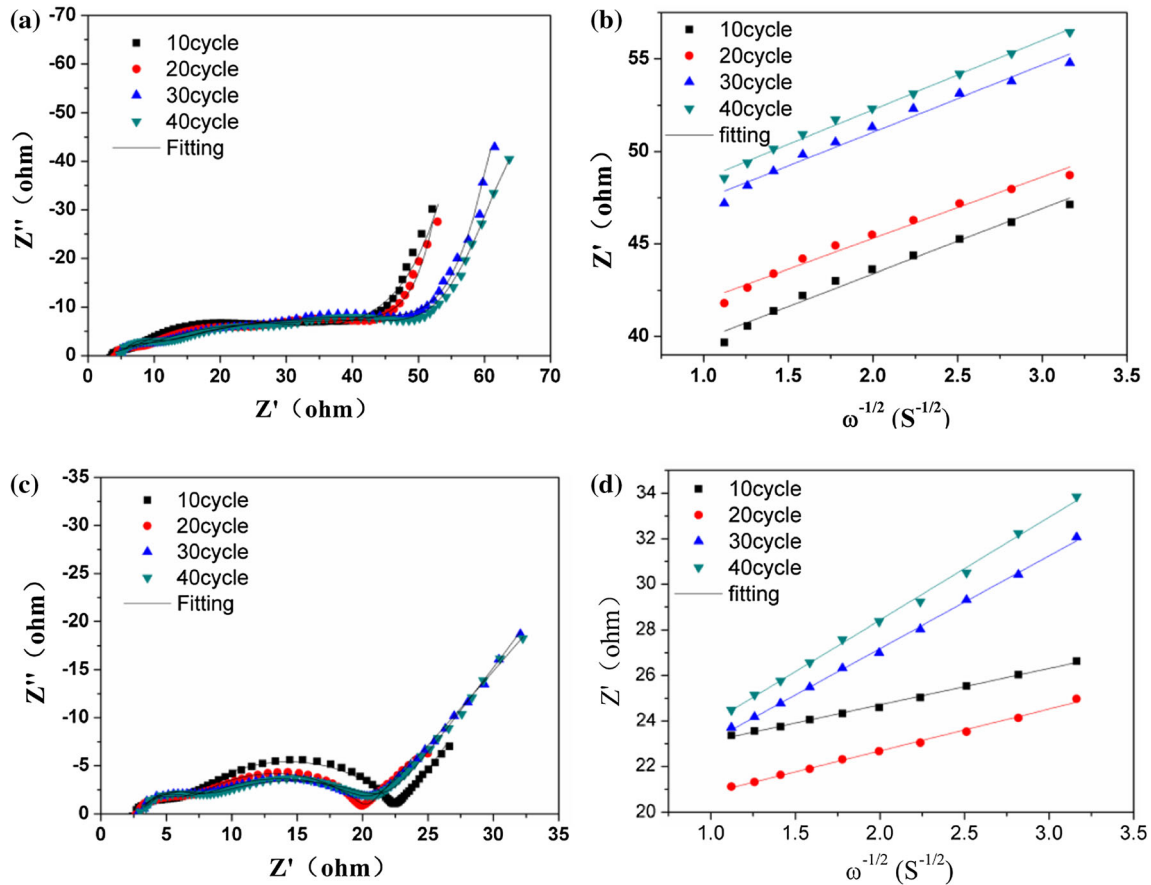


**Figure 7** **a** Nyquist plots of G@Si composite after different cycles; **b** the relationship between  $Z'$  and  $\omega^{-1/2}$  in low-frequency region derived from **a**; **c** Nyquist plots of G@Si@C composite

after different cycles; **d** the relationship between  $Z'$  and  $\omega^{-1/2}$  in low-frequency region derived from **c**.

**Table 2** Kinetic parameters of G@Si composite and G@Si@C composite electrodes after different cycles

Sample	Cycle number	$R_s$ ( $\Omega$ )	$R_f$ ( $\Omega$ )	$R_{ct1}$ ( $\Omega$ )	$R_{ct2}$ ( $\Omega$ )	Slope
G@Si composite	10	3.64	1.76	22.33	17.95	3.52
	20	4.25	2.45	16.84	21.64	3.33
	30	4.66	3.02	14.20	22.43	3.63
	40	4.99	3.53	12.43	24.93	3.74
Sample	Cycle number	$R_s$ ( $\Omega$ )	$R_f$ ( $\Omega$ )	$R_{ct}$ ( $\Omega$ )	Slope	
G@Si@C composite	10	2.46	2.33	15.69		1.60
	20	3.04	2.80	14.92		1.84
	30	3.15	2.81	14.42		4.07
	40	3.34	2.83	13.88		4.52

means the fast lithium-ion diffusion kinetics inside the electrode [50]. The carbon layer improves the charge transfer, which is benefit to lithium-ion diffusion behavior in the electrode, so the slope of G@Si@C composite electrode at 10th and 20th cycle is lower than G@Si composite electrode. The SEI film

impedes lithium-ion diffusion behavior in the electrode, so the slope rises with the increase in cycle number. The electrochemistry kinetic performance charge transfer and lithium-ion diffusion ability decide the high-rate discharge ability. The G@Si@C composite electrode shows preferable

electrochemistry kinetic performance, which is in accordance with the fine high-rate discharge ability.

## Conclusions

The G@Si composite precursor has been obtained by an industrial spray drying method. The core-shell asphalt-carbon-coated G@Si@C composite has been successfully prepared by fast fusing an asphalt layer formed on the surface of G@Si composite precursor and carbonizing at 1100 °C for 2 h. A carbon layer on the surface of G@Si@C composite and the nano-Si particle is pinned on the graphite surface without bareness. The initial reversible charge capacity and coulombic efficiency of G@Si@C composite are 502.5 mAh g<sup>-1</sup> and 87.5%, respectively, with the charge capacity retention of 83.4% after 400 cycles. The carbon layer can relieve volume change and stable SEI film. Moreover, the particle pulverization can also be inhibited, which is benefit to improve the cycle performance. The carbon layer can enhance the electrical conductivity and the electrochemical kinetics of G@Si@C composite, so the high-rate discharge ability is superior.

## Acknowledgements

This work was supported by the Guangxi Innovation-Driven Development Project (AA17204022, AA18118001), the Science and Technology Plan of China Nonferrous Group (2016KJJH03) and the Scientific and Technological Plan of Guilin City (201607010322).

## Compliance with ethical standards

**Conflict of interest** The authors declare that they have no conflict of interest.

## References

- [1] Lu J, Chen Z, Pan F, Cui Y, Amine K (2018) High-performance anode materials for rechargeable lithium-ion batteries. *Electrochem Energy Rev* 1:35–53
- [2] Dou F, Shi L, Chen G, Zhang D (2019) Silicon/carbon composite anode materials for lithium-ion batteries. *Electrochem Energy Rev* 2:149–198
- [3] Wang B, Li W, Wu T, Guo J, Wen Z (2018) Self-template construction of mesoporous silicon submicrocube anode for advanced lithium ion batteries. *Energy Storage Mater* 15:139–147
- [4] Yu ZZ, Tian BB, Li Y, Fan DY, Yang DG, Zhu GS, Cai M, Yan DL (2019) Lithium titanate matrix-supported nanocrystalline silicon film as an anode for lithium-ion batteries. *ACS Appl Mater Interfaces* 11:534–540
- [5] Hassan FM, Chabot V, Elsayed AR, Xiao X, Chen Z (2014) Engineered Si electrode nano architecture: a scalable post fabrication treatment for the production of next-generation Li-ion batteries. *Nano Lett* 14:277–283
- [6] Xue JS, Dahn JR (1995) An epoxy-silane approach to prepare anode materials for rechargeable lithium-ion batteries. *J Electrochem Soc* 142:2927–2935
- [7] Wilson AM, Dahn JR (1995) Lithium insertion in carbons containing nano-dispersed silicon. *J Electrochem Soc* 142:326–332
- [8] Chan KY, Wolverton C, Greeley JP (2012) First principles simulations of the electrochemical lithiation and delithiation of faceted crystalline silicon. *JACS* 134:14362–14374
- [9] Zhang Z, Liao NB, Zhou HM, Xue W (2019) Insight into silicon-carbon multilayer films as anode materials for lithium-ion batteries: a combined experimental and first principles study. *Acta Mater* 178:173–178
- [10] Wang MY, Yin L, Li MQ, Luo SH, Wang C (2019) Low-cost heterogeneous dual-carbon shells coated silicon monoxide porous composites as anodes for high-performance lithium-ion batteries. *J Colloid Inter Sci* 549:225–235
- [11] Li JY, Xu Q, Li G, Yin YX, Wan LJ, Guo YG (2017) Research progress regarding Si-based anode materials towards practical application in high energy density Li-ion batteries. *Mater Chem Front* 1:1691–1708
- [12] Lu ZD, Liu N, Lee HW, Zhao J, Li WY, Li YZ, Cui Y (2015) Nonfilling carbon coating of porous silicon micrometer-sized particles for high-performance lithium battery anodes. *ACS Nano* 9:2540–2547
- [13] Dong QC, Yang J, Wu MY, Zhou XY, Zhang YZ, Wang WJ, Si WL (2018) Template-free synthesis of cobalt silicate nanoparticles decorated nanosheets for high performance lithium ion batteries. *ACS Sustain Chem Eng* 6:15591–15597
- [14] Fang M, Wang Z, Chen X, Guan S (2018) Sponge-like reduced graphene oxide/silicon/carbon nanotube composites for lithium ion batteries. *Appl Surf Sci* 436:345–353
- [15] Li Y, Chang B, Li T, Kang L, Xu S, Zhang D, Xie L, Liang W (2016) One-step synthesis of hollow structured Si/C composites based on expandable microspheres as anodes for lithium ion batteries. *Electrochem Commun* 72:69–73

- [16] Sun CF, Zhu H, Okada M, Gaskell K, Inoue Y (2015) Interfacial oxygen stabilizes composite silicon anodes. *Nano Lett* 15:703–708
- [17] Aliya M, Albina J, Myung ST, Kim SS (2018) A mini-review on the development of Si-based thin film anodes for Li-ion batteries. *Mater Today Energy* 9:49–66
- [18] Lucas AB, Lee SW, Cui Y, William DN (2015) Mechanical behavior of electrochemically lithiated silicon. *J Power Sources* 273:41–51
- [19] Zhang F, Yang X, Xie Y, Yi N, Huang Y, Chen Y (2015) Pyrolytic carbon-coated Si nanoparticles on elastic graphene framework as anode materials for high-performance lithium-ion batteries. *Carbon* 82:161–167
- [20] Javier B, Ilya AS, James AG, Matilda K, Daniel PA (2017) Capacity fade and its mitigation in Li-ion cells with silicon-graphite electrodes. *J Phys Chem C* 121:20640–20649
- [21] Roy AK, Zhong M, Schwab MG, Binder A, Venkataraman SS, Tomovic Z (2016) Preparation of a binder-free three-dimensional carbon foam/silicon composite as potential material for lithium ion battery anodes. *ACS Appl Mater Inter* 8:7343–7348
- [22] Luo W, Wang YX, Wang LJ, Jiang W, Chou SL, Dou SX (2016) Silicon/mesoporous carbon/crystalline TiO<sub>2</sub> nanoparticles for highly stable lithium storage. *ACS Nano* 10:10524–10532
- [23] Hwa Y, Kim WS, Yu BC, Hong SH (2013) Enhancement of the cyclability of a Si anode through Co<sub>3</sub>O<sub>4</sub> coating by the Sol–Gel method. *J Phys Chem C* 117:7013–7017
- [24] Li G, Li JY, Yue FS, Xu Q, Zuo TT, Yin YX (2019) Reducing the volume deformation of high capacity SiOx/G/C anode toward industrial application in high energy density lithium-ion batteries. *Nano Energy* 60:485–492
- [25] Zhu LH, Chen YL, Wu CQ (2020) Double-carbon protected silicon anode for high performance lithium-ion batteries. *J Alloy Compd* 812:151848–151855
- [26] Huang HJ, Rao PH, Choi WM (2019) Carbon-coated silicon/crumpled graphene composite as anode material for lithium-ion batteries. *Curr Appl Phys* 19:1349–1354
- [27] Lu J, Chen ZW, Pan F, Cui Y, Amine K (2018) High-performance anode materials for rechargeable lithium-ion batteries. *Electrochem Energy Rev* 1:35–53
- [28] Dou F, Shi LY, Chen GR, Zhang DS (2019) Silicon/carbon composite anode materials for lithium-ion batteries. *Electrochem Energy Rev* 2:149–198
- [29] Jin Y, Zhu B, Lu ZD, Liu NA, Zhu J (2017) Challenges and recent progress in the development of Si anodes for lithium-ion battery. *Adv Energy Mater* 7:1700715
- [30] Chen HD, Wang ZL, Hou XH, Fu LJ, Wang SF, Hu XQ, Qin HQ, Wu YP, Ru Q (2017) Mass-producible method for preparation of a carbon-coated graphite@plasma nano-silicon@carbon composite with enhanced performance as lithium ion battery anode. *Electrochim Acta* 249:113–121
- [31] Chen HD, Hou XH, Chen FM, Wang SF, Wu B, Ru Q, Qin HQ (2018) Milled flake graphite/plasma nano-silicon@carbon composite with void sandwich structure for high performance as lithium ion battery anode at high temperature. *Carbon* 130:433–440
- [32] Wang GQ, Xu B, Shi JG, Lei XL, Ouyang CY (2018) Confined Li ion migration in the silicon-graphene complex system: an ab initio investigation. *Appl Surf Sci* 436:505–510
- [33] Xiaoqiao Hu, Huang Shimin, Hou Xianhua, Chen Hedong, Qin Haiqing, Qiang Ru (2018) A double core-shell structure silicon carbon composite anode material for a lithium ion battery. *Silicon* 10:1443–1450
- [34] Zhou Y, Tian Z, Fan R, Zhao S, Zhou R, Guo H, Wang Z (2015) Scalable synthesis of Si/SiO<sub>2</sub>@C composite from micro-silica particles for high performance lithium battery anodes. *Powder Technol* 284:365–370
- [35] Zhou Y, Guo HJ, Wang ZX, Li XH (2017) Improved electrochemical performance of Si/C material based on the interface stability. *J Alloy Compd* 725:1304–1312
- [36] So KS, Lee HJ, Kim TH (2014) Synthesis of silicon nanopowder from silane gas by RF thermal plasma. *Phys Status Solidi A* 211:310–315
- [37] Chen HD, Hou XH, Qu LN, Qin HQ, Ru Q (2017) Electrochemical properties of core-shell nano-Si@carbon composites as superior anode materials for high-performance Li-ion batteries. *J Mater Sci: Mater Electron* 28:250–258
- [38] Yana M, David Z (2017) Operando plasmon-enhanced Raman spectroscopy in silicon anodes for Li-ion battery. *J Nanopart Res* 19:372
- [39] Wang M, Xiao X (2016) Investigation of the chemo-mechanical coupling in lithiation/delithiation of amorphous Si through simulations of Si thin films and Si nanospheres. *J Power Sources* 326:365–376
- [40] He D, Huang X, Li M (2019) Hierarchical C-P(=O)(-O-)<sub>n</sub> (n<2)-linked nano-Si/Ndoped C/graphene porous foam as anodes for high-performance lithium ion batteries. *Carbon* 141:531–541
- [41] Kaushik K, Marco-Tulio FR, Stephen ET, Ilya AS (2018) Calendar-life versus cycle-life aging of lithium-ion cells with silicon-graphite composite electrodes. *Electrochim Acta* 280:221–228
- [42] Kaushik K, Ilya AS, Richard TH, Cameron P (2017) Auger electrons as probes for composite micro- and nanostructured materials: application to solid electrolyte interphases in graphite and silicon-graphite electrodes. *J Phys Chem C* 121:23333–23346



- [43] Liu NT, Liu J, Jia DZ, Huang YD (2019) Multi-core yolk-shell like mesoporous double carbon-coated silicon nanoparticles as anode materials for lithium-ion batteries. *Energy Storage Mater* 18:165–173
- [44] Zhou Y, Guo H, Yong Y, Wang Z, Li X, Zhou R (2017) Introducing reduced grapheme oxide to improve the electrochemical performance of silicon-based materials encapsulated by carbonized polydopamine layer for lithium ion batteries. *Mater Lett* 195:164–167
- [45] Chen HD, Shen KX, Hou XH, Zhang GZ (2019) Si-based anode with hierarchical protective function and hollow ring-like carbon matrix for high performance lithium ion batteries. *Appl Surf Sci* 470:496–506
- [46] He W, Tian HJ, Xin FX, Han WQ (2015) Scalable fabrication of micro-sized bulk porous Si from Fe-Si alloy as a high performance anode for lithium-ion batteries. *J Mater Chem A* 3:17956–17962
- [47] Zhou Y, Guo HJ, Yan GC, Wang ZX (2018) Fluidized bed reaction towards crystalline embedded amorphous Si anode with much enhanced cycling stability. *Chem Commun* 54:3755–3758
- [48] Liang GM, Qin XY, Zou JS, Luo LY, Wang YZ (2018) Electrospayed silicon-embedded porous carbon microspheres as lithium-ion battery anodes with exceptional rate capacities. *Carbon* 127:424–431
- [49] Yi Z, Lin N, Xu TJ, Qian YT (2018) TiO<sub>2</sub> coated Si/C interconnected microsphere with stable framework and interface for high-rate lithium storage. *Chem Eng J* 347:214–222
- [50] Maciej R, Bartosz H, Michał K, Maciej B (2018) The effect of compressive stresses on a silicon electrode's cycle life in a Li-ion battery. *RSC Adv* 8:22546–22551

**Publisher's Note** Springer Nature remains neutral with regard to jurisdictional claims in published maps and institutional affiliations.